

Optimization of aperiodic dielectric structures

Philip Seliger

Department of Mathematics, University of Southern California, 3620 S. Vermont Avenue, KAP 246, Los Angeles, California 90089-1113

Mohammad Mahvash

Department of Electrical Engineering, University of Southern California, 3620 S. Vermont Avenue, KAP 132, Los Angeles, California 90089-2533

Chunming Wang

Department of Mathematics, University of Southern California, 3620 S. Vermont Avenue, KAP 246, Los Angeles, California 90089-1113

A. F. J. Levi^{a)}

Department of Electrical Engineering, University of Southern California, 3620 S. Vermont Avenue, KAP 132, Los Angeles, California 90089-2533

(Received 1 November 2005; accepted 5 June 2006; published online 8 August 2006)

The electromagnetic scattering properties of identical parallel dielectric cylinders configured to closely match a desired response are investigated. Spatial arrangements obtained using a computationally efficient gradient-based optimizer and finite difference forward solver are aperiodic and nonintuitive. We find good agreement between calculations and experiments performed at 37.5 GHz and suggest that finite-sized aperiodic configurations may provide access to functionality inaccessible by conventional periodic, photonic crystal inspired, designs. © 2006 American Institute of Physics. [DOI: [10.1063/1.2221497](https://doi.org/10.1063/1.2221497)]

I. INTRODUCTION

The study of photonic crystals¹ (PCs) is inspired, in part, by a desire to seek compact designs for optical and rf components. Much work has focused on two-dimensional (2D) periodic dielectric structures due to availability of planar fabrication techniques. However, there are a number of fundamental issues that appear to be impediments to adoption of PCs as a technology. These include the fact that the inherent spatial periodicity of the PC structure results in limited functionality. Often one must break spatial symmetry to obtain a useful device response. For example, waveguides are typically created by introducing a line defect and filters might make use of one or more point defects. Hence, one may make the observation that usually a desired functionality requires breaking the underlying spatial symmetry of the periodic dielectric structure. Even in situations where one wishes to access properties intrinsic to periodic dielectrics such as nonlinear dispersion, coupling electromagnetic radiation from free space, and finite-size effects present significant challenges.²

One approach that attempts to circumvent such difficulties is application of optimization techniques to PCs.^{3–6} On the one hand, such numerical studies are usually limited to a finite number of identical dielectric scatterers whose broken symmetry spatial distribution is restricted to periodic PC lattice positions. On the other hand, they benefit from the fact that a less biased search of solution space can result in non-intuitive optimized designs. Our initial approach⁷ has been to retain identical dielectric scatterers but to remove all bias to periodic PC inspired designs. In this way adaptive algorithms

can seek optimal solutions in a much larger space of *aperiodic* dielectric structures and hence, at least, in principle, access a larger range of functionalities.

The purpose of this paper is to describe our approach to efficient optimization of aperiodic configurations and to report on the experimental verification of our initial designs. Laboratory measurements are performed using millimeter wave electromagnetic (EM) radiation at frequency $f_0 = 37.5$ GHz corresponding to free-space wavelength $\lambda_0 = 8$ mm. Because electromagnetic waves scattering from nonmagnetic lossless dielectric is determined by the Helmholtz equation, our approach scales with frequency and hence may be applied to the design of nanophotonic devices.

II. ELECTROMAGNETIC SOLVER

We begin by noting that the objective or target response is, in general, a function of the EM field. For our prototype problem we are interested in relative EM power distribution on a measurement curve. Even though the objective response is specified in a limited region of the device, the forward problem is solved over the entire modeling domain. The quasi-2D geometry of typical PCs as well as efficiency considerations led us to implement a 2D EM field solver. Our experiments performed at millimeter wave frequencies also use a 2D geometry. Figure 1(a) shows the basic experimental arrangement in which a $f_0 = 37.5$ GHz rf signal is introduced into a waveguide whose 7×3.5 mm² aperture is attached to a metal horn. The EM power distribution is detected using a probe that can move to angle θ on a radius $r_s = 60$ mm. This defines a measurement curve, s . To maintain the 2D nature of the EM experiment, the total structure is sandwiched between two metal plates separated by 3.5 mm $< \lambda_0/2$. The

^{a)}Electronic mail: alevi@usc.edu

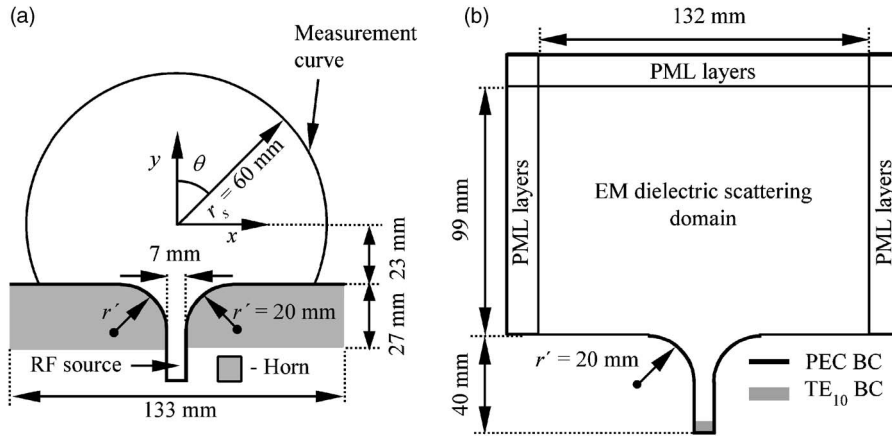


FIG. 1. (a) Top view of experimental layout showing physical dimensions. EM power from a rf source of frequency $f_0=37.5$ GHz is fed via a waveguide and horn. The measurement curve is indicated. In the experiments, EM power is measured as a function of θ on this curve. (b) Domain decomposition of the FD EM simulation. PML layers of finite thickness are truncated with a PEC boundary condition. The waveguide introduces the EM beam as a fixed TE₁₀ mode EM field on the indicated boundary.

prototype problem we choose to study has an objective response in which the incident EM radiation propagating in the $\theta=0^\circ$ direction is scattered into a top-hat function whose peak on the measurement curve occurs over the angular range $30^\circ \leq \theta \leq 60^\circ$.

The forward problem we consider describes the propagation of the EM wave over the domain illustrated in Fig. 1(b). This EM dielectric scattering domain contains the dielectric scatters whose spatial arrangement we wish to optimize. Since stationary solutions at a single frequency are sought we consider Maxwell's equations in the frequency domain, eliminating the time variable. When only dielectric material is present and no currents flow, Maxwell's equations simplify further. The magnetic field can be eliminated to yield

$$\nabla \times (\mu_0 \mu_r)^{-1} \cdot \nabla \times \mathbf{E} - \omega_0^2 \epsilon_0 \epsilon_r \mathbf{E} = 0, \quad (1)$$

where \mathbf{E} is the electric field, $\omega_0 = 2\pi f_0$, ϵ_0 is the permittivity of free space, ϵ_r is relative permittivity, μ_0 is the permeability of free space, and μ_r is the relative permeability. One boundary condition (BC) is that $|\mathbf{E}|=0$ inside metal, so we treat metal as a perfect electric conductor (PEC). Waves leaving the EM dielectric scattering domain that are not bounded by metal have $|\mathbf{E}| \rightarrow 0$ as $\mathbf{r} \rightarrow \infty$. When simulating the 2D EM scattering experiment, the TE₁₀ mode of the waveguide is excited and acts as the source of EM radiation. This is modeled using a Dirichlet BC [TE₁₀ BC in Fig. 1(b)]. In this situation only the z component of electric field E_z propagates in the system and (1) reduces to

$$[\partial_x(\mu_r^{-1} \partial_x) + \partial_y(\mu_r^{-1} \partial_y)]E_z + \omega_0^2 \mu_0 \epsilon_0 \epsilon_r E_z = 0. \quad (2)$$

The partial differential equation (PDE) (2) may be used to describe scattering of an EM wave by dielectric cylinders that are represented by a relative permittivity distribution $\epsilon_{r_z}(x, y)$. We consider a 2D configuration of Teflon scattering cylinders, each with a diameter 3.175 ± 0.025 mm. Teflon is modeled as a lossless dielectric with $\mu_r=1$ and a real valued relative permittivity $\epsilon_{r_z}=2.05$ in (2). In this situation (2) is identical to the scalar Helmholtz equation over the EM dielectric scattering domain indicated in Fig. 1(b).

The EM waves can propagate into open space beyond the EM dielectric scattering domain. Since total energy is finite, the magnitude of EM waves must tend to zero as the propagation distance tends to infinity. Simulation of the open

space by a bounded domain is achieved using perfectly matched layers^{8,9} (PMLs) consisting of an artificial material with varying complex permeability and permittivity in (2). The PMLs are designed to simulate a perfectly absorbing medium.

We solve the scattering problem numerically by approximating the PDE in (2) with the finite difference (FD) equation for $E_{z,i,j}$,

$$\begin{aligned} & \left\{ -\frac{1}{\Delta^2} (\mu_{r_y, i+1/2, j}^{-1} + \mu_{r_y, i-1/2, j}^{-1} + \mu_{r_x, i, j+1/2}^{-1} + \mu_{r_x, i, j-1/2}^{-1}) \right. \\ & \quad \left. + \omega_0^2 \mu_0 \epsilon_0 \epsilon_{r_z, i, j} \right\} E_{z, i, j} + \frac{1}{\Delta^2} \mu_{r_y, i+1/2, j}^{-1} E_{z, i+1, j} \\ & \quad + \frac{1}{\Delta^2} \mu_{r_y, i-1/2, j}^{-1} E_{z, i-1, j} + \frac{1}{\Delta^2} \mu_{r_x, i, j+1/2}^{-1} E_{z, i, j+1} \\ & \quad + \frac{1}{\Delta^2} \mu_{r_x, i, j-1/2}^{-1} E_{z, i, j-1} = 0, \end{aligned} \quad (3)$$

where $E_{z,i,j}$ is the approximated value of $E_z(x_i, y_j)$ and (x_i, y_j) are evenly spaced square-grid points with step size $\Delta \leq \lambda_0/20$. Equation (3) is satisfied at all interior points of the EM dielectric scattering domain and the PML area. Dirichlet conditions are satisfied at boundary points as shown in Fig. 1(b). We chose the FD method because of the relative ease with which it can solve for arbitrary geometry and, in particular, the PEC metal horn used to launch the EM wave.

When values $E_{z,i,j}$ are ordered into a column vector, Eq. (3) can be written in matrix notation as

$$\mathbf{L} \cdot \mathbf{E}_z = \mathbf{b}, \quad (4)$$

where \mathbf{L} is the complex-valued sparse FD matrix including the formulation of the PML absorbing boundary, \mathbf{E}_z are the unknown complex electric field values, and \mathbf{b} contains the boundary conditions in the FD equation.

The power of EM waves at any point on the measurement curve can be derived from the solution of (4). More precisely, the power of EM waves is initially computed at all grid points. The power on the measurement curve is then obtained by interpolation. For a point on the measurement curve defined by angle θ , the nearest four grid points are denoted by $\{x_{i_1, j_1}, x_{i_2, j_2}, x_{i_3, j_3}, x_{i_4, j_4}\}$ and the modeled EM power is proportional to

$$s_{\text{mod}}(\theta) = \sum_{k=1}^4 w_k(\theta) |E_{z,i_k,j_k}|^2. \quad (5)$$

We use standard Gaussian weights at position (x, y) given by

$$w_k = \exp\{-[(x - x_{i_k})^2 + (y - y_{j_k})^2]/4\Delta^2\}/C,$$

where $C = \sum_{k=1}^4 \exp\{-[(x - x_{i_k})^2 + (y - y_{j_k})^2]/4\Delta^2\}$. Gaussian weight in smoothing of a function of two (or more) variables is as computationally efficient as bilinear interpolation with the additional advantage of avoiding faceted interpolated surfaces.

Defining a row-vector valued function $\mathbf{W}(\theta)$ with only four nonzero entries that are associated with neighboring grid points yields

$$s_{\text{mod}}(\theta) = \mathbf{W}(\theta) \cdot \text{diag}(\mathbf{E}_z) \mathbf{E}_z^*. \quad (6)$$

Comparison of calculated EM power profile along the measurement curve with experimental results serves to verify the FD method.

III. COST FUNCTIONAL

As a measure of the fitness of a given configuration with respect to the design objectives we define a scalar cost functional J . The cost functional measures how well the modeled EM profile s_{mod} along the measurement curve matches the desired profile s_{obj} . In the design problem we consider s as relative power but it can represent any other feature of the EM field, such as Poynting vector or complex electric field if control of the phase is desired. In our prototype problem function $s_{\text{mod}}(\theta)$ is discretized into M sample points. The cost functional is

$$J = \sum_{k=1}^M m_k |s_{\text{mod}}(\theta_k) - s_{\text{obj}}(\theta_k)|^{\gamma_k} \quad (7)$$

subject to the constraints that E_z satisfies Maxwell's equations given by $\mathbf{L}(\mathbf{p}) \cdot \mathbf{E}_z = \mathbf{b}$ and $s_{\text{mod}}(\theta) = \mathbf{W}(\theta) \cdot \text{diag}(\mathbf{E}_z) \mathbf{E}_z^*$ [Eqs. (4) and (6)]. Minimizing the cost functional over possible parameter settings \mathbf{p} yields an optimized design. In particular, \mathbf{p} contains the coordinates of the scattering cylinder centers and determines $\varepsilon_{r_z,i,j}$ in the FD equation (3). Other design considerations such as robustness against small variations in parameters could also be translated into additional terms in J . The linear weight $m(\theta)$ and the exponent $\gamma(\theta) > 1$ allow flexibility in placing emphasis on design aspects of the power profile along the measurement curve. For example, focusing 95% of the power onto the measurement curve might demand compromises in the shape of the focused power profile. The modeled power distribution $s_{\text{mod}}(\theta)$ might not form a perfect top hat. In this case one might increase the linear weight m and possibly lower the value of the exponent γ for angles within the top-hat peak to improve the solution. We note that J is only indirectly a function of the design parameters \mathbf{p} which explicitly appear in the FD matrix \mathbf{L} .

IV. GRADIENT-BASED OPTIMIZATION USING THE ADJOINT METHOD

Efficient local optimization techniques require evaluation of the gradient of the cost functional with respect to the design parameters. Since the relative permittivity coefficient ε_{r_z} is not a differentiable function with respect to the position of the dielectric cylinders, the solution \mathbf{E}_z is not differentiable with respect to the position. In our implementation, permittivity at a grid point is taken to be the average value of ε_{r_z} enclosed by a circle of radius Δ centered at the grid point. This effectively smoothes out the discontinuity in ε_{r_z} . Local averaging maintains the mathematical consistency of the FD method while providing differentiability of the solution with respect to the cylinder positions. Such local averaging is appropriate for our computationally efficient fixed-grid implementation. The smoothing in the finite difference method allows analytic computation of the gradient using the adjoint method. The gradient of the cost functional $\nabla_{\mathbf{p}} J = (\partial_{p_1} J, \dots, \partial_{p_{2n}} J)$ is evaluated using $\partial_{p_i} J = -2 \text{Re}(\mathbf{F}^H \cdot (\partial_{p_i} \mathbf{L} \cdot \mathbf{E}_z))$ in which \mathbf{F} is the solution of the adjoint equation (8),

$$\mathbf{L}(\mathbf{p})^H \mathbf{F} = \text{diag}(\mathbf{E}_z) \cdot \left\{ \sum_{k=1}^M m_k \gamma_k [s_{\text{mod}}(\theta_k) - s_{\text{obj}}(\theta_k)]^{\gamma_k - 1} \mathbf{W}(\theta_k)^H \right\}. \quad (8)$$

In Eq. (8), H indicates conjugate transpose. The cost of computing the matrix derivatives $\partial_{p_i} \mathbf{L}$ grows linearly in the number of design parameter p_i but evaluation of these derivatives adds little to the overall computational effort.

For local optimization we implement a modified gradient method. Cylinder overlap is not allowed which does represent an important constraint during the iterative optimization procedure. In our implementation, colliding cylinders are moved apart a distance $\lambda_0/8$ prior to continued optimization.

V. RESULTS

We verify our numerical simulations by performing experiments. The detected power profile along the measurement curve is compared to the calculated power profile. As an initial test, a 5×5 finite-sized periodic array of cylindrical dielectric scatters with lattice constant equal to the free-space wavelength, λ_0 , was studied. This is described in Sec. V A. Section V B describes results of an optimized aperiodic structure.

A. Finite-sized periodic structure

Figure 2(a) is a photograph of 25 Teflon cylinders arranged in a 5×5 finite-sized periodic array and attached to a metal slab that forms the lower half of a waveguide with upper metal plate removed. The Teflon cylinders have a measured diameter of 3.175 ± 0.025 mm and $\varepsilon_{r_z} = 2.05$. Experiments to measure EM power are performed with the upper half of the metal waveguide attached. EM power reaching the measurement curve is detected using a small dipole antenna feeding a narrow-band amplifier.

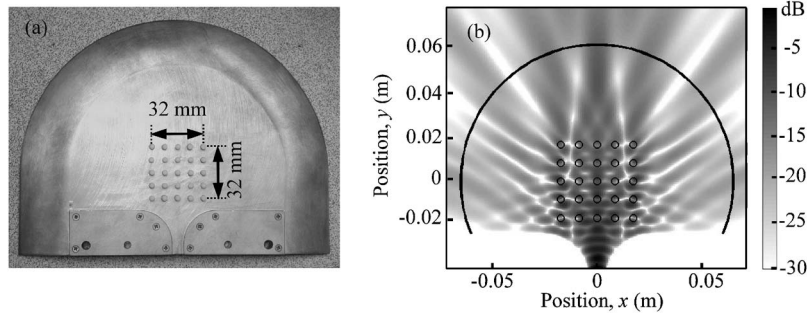


FIG. 2. (a) Photograph showing top view of 25 Teflon cylinders arranged in a 5×5 finite-sized periodic array and attached to a metal slab that forms the lower half of a waveguide. The upper metal plate of the EM waveguide is removed. (b) Calculated relative EM power at frequency $f_0=37.5$ GHz in the dielectric scattering domain. The gray scale is in decibels. EM radiation emerging from the metal horn is incident on a 5×5 finite-sized lattice of dielectric cylinders. The dielectric cylinders are 3.175 ± 0.025 mm in diameter and are placed symmetrically about the origin with lattice spacing λ_0 . The relative permittivity of the Teflon cylinders is $\epsilon_r=2.05$. The solid line is the measurement curve.

Figure 2(b) shows the power distribution at frequency $f_0=37.5$ GHz calculated using the method described in Sec. II. In Fig. 2(b), the gray scale indicates relative EM power measured in units of decibels. The calculations show a diffraction pattern that is symmetric about the $\theta=0^\circ$ line. This is to be expected for the periodic array. In addition, there is interference between EM waves emanating from the dielectric array and subsequently reflected from the metal horn.

Figure 3(a) shows a comparison between calculated and detected EM power as a function of angle θ on the measurement curve, s . The relative power scale is linear. As may be seen, agreement between calculated and measured data is good with all the main features appearing in both data. Figure 3(b) is the same data as in Fig. 3(a) but with relative EM power plotted on a logarithmic scale. Here, the excellent agreement for the three main peaks and the -30 dB minima at $\pm 40^\circ$ is apparent. A slight asymmetry in the measured data also exists whose origin is likely due to dielectric cylinder placement errors that are measured to have a standard deviation less than $100 \mu\text{m}$.

The overall agreement between calculated and measured results gives us confidence to consider the optimization of aperiodic dielectric structures.

B. Aperiodic dielectric structure for a top-hat objective function

As our prototype problem we seek an objective response in which the maximum amount of incident EM radiation propagating in the $\theta=0^\circ$ direction is scattered into a top-hat function defined on the measurement curve in Fig. 1(a) and

whose peak occurs in the angular range $30^\circ \leq \theta \leq 60^\circ$. Symmetrically placed structures, such as the 5×5 finite-sized periodic array discussed in Sec. V A, are unable to provide the desired functionality. However, one anticipates broken symmetry spatial arrangements of dielectric scatters will do better.

Rather than attempt to adapt *ad hoc* PC-inspired designs, we used the search algorithm described in Secs. II–IV to find the optimal spatial configuration of 50 identical Teflon dielectric cylinders. The result is a nonintuitive aperiodic distribution.

Figure 4(a) is a photograph of the experimental arrangement. As may be seen, the positions of the Teflon cylinders do not have any obvious spatial symmetry. Figure 4(b) shows the calculated relative EM power at frequency $f_0=37.5$ GHz. The gray scale is in decibels and the solid line is the measurement curve. EM radiation from the metal horn is incident on the 50 dielectric cylinders in the dielectric scattering domain. Figure 4(c) shows the desired (broken curve) and modeled (solid curve) power profile along the measurement curve. 95.0% of the calculated EM power reaching the measurement curve in the angular range $-90^\circ \leq \theta \leq 90^\circ$ is focused under the $30^\circ \leq \theta \leq 60^\circ$ top-hat peak. The ripples in the top-hat's power as a function of θ are 1.45 dB peak to peak. Figure 4(d) is the same as Fig. 4(c) but power is on a logarithmic scale (decibel).

Figure 5(a) shows calculated and detected relative EM power profile along the measurement curve. The relative power scale is linear. As with the finite-sized periodic array discussed in Sec. V A, agreement between experiment and calculation is good. Figure 5(b) is the same as Fig. 5(a) but

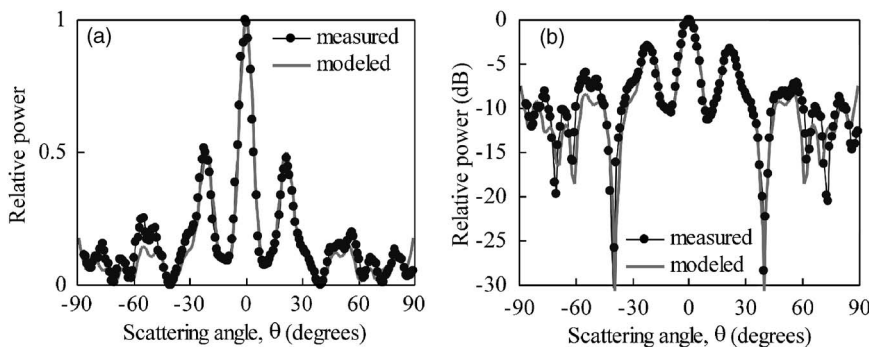


FIG. 3. (a) Calculated and detected relative EM power {defined by $s(\theta)/\max_{-90 \leq \phi \leq 90}[s(\phi)]$ } as a function of angle θ on the measurement curve. (b) Same as (a) but relative power is on a logarithmic scale (decibel).

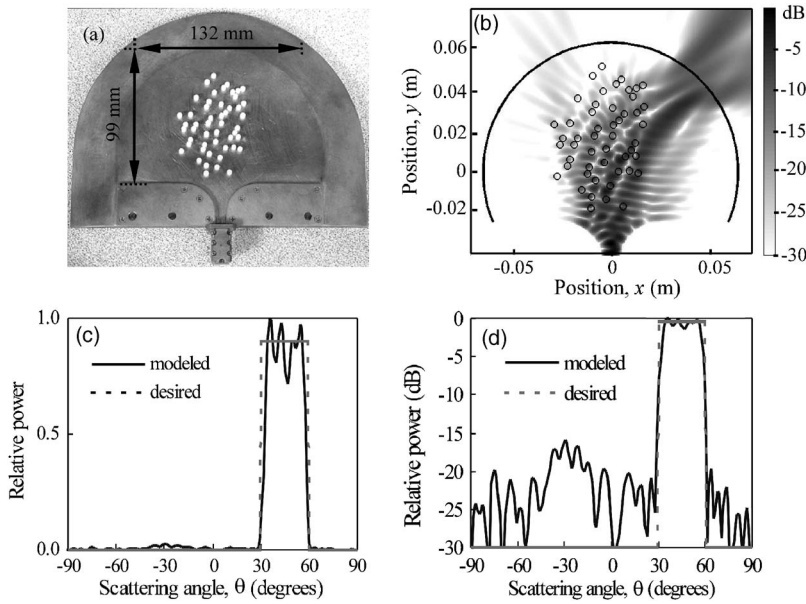


FIG. 4. (a) Photograph showing top view of aperiodic dielectric array attached to lower metal plate that forms the lower half of an EM waveguide. The upper metal plate of the EM waveguide is removed. (b) Calculated relative EM power at frequency $f_0=37.5$ GHz. The gray scale is in units of decibel. EM radiation from the metal horn is incident on 50 dielectric cylinders in the dielectric scattering domain. The dielectric cylinders are 3.175 ± 0.025 mm in diameter and $\epsilon_r=2.05$. The cylinder positions are optimized to focus EM power on the measurement curve under a top-hat function which peaks between angles $30^\circ \leq \theta \leq 60^\circ$. The measurement curve is shown as a solid line. (c) The desired and modeled power profile along the measurement curve. 95% of the calculated EM power reaching the measurement curve is focused under the top-hat peak. The ripples in the top-hat's power as a function of θ are 1.45 dB peak to peak. (d) Same as (c) but power is on a logarithmic scale (decibels).

the relative power scale is logarithmic and measured in decibels. Ripples at the top-hat peak are approximately 1.77 dB peak to peak. This is only 0.32 dB greater than the calculated value. The portion of the measured power focused between scattering angles $30^\circ \leq \theta \leq 60^\circ$ in the range $-90^\circ \leq \theta \leq 90^\circ$ is 92.4%. This is slightly less than the calculated value of 95.0%. The measured relative EM power reflected back into the waveguide is $S_{11}=-20$ dB.

C. Sensitivity analysis

Practical device design must be robust against variations in spatial configuration introduced during manufacture. The robustness of an optimal design is closely associated with performance degradation as a function of perturbation of the design parameters. Performance degradation can greatly vary for perturbations with the same Euclidian distance to the optimal design. When the cost functional is twice differentiable, the direction of maximal sensitivity is characterized by the eigenvector associated with the largest eigenvalue of the Hessian matrix. However, for our prototype problem, evaluation of the Hessian matrix can be computationally challenging.

Instead of evaluating the local Hessian we compared the robustness of the 5×5 finite-sized periodic array and the optimized aperiodic structure with respect to a uniform random perturbation of size L centered around each scattering site. As a measure of the robustness of the power profile we

evaluated the standard deviation $\sigma(J')$ where $J'(\mathbf{p}^{\text{pert}}) = \{\sum_{k=1}^M [s_{\text{mod}}(\theta_k, \mathbf{p}^{\text{pert}}) - s_{\text{mod}}(\theta_k, \mathbf{p}^0)]^2\}^{1/2}$, and \mathbf{p}^{pert} is the uniform perturbation of \mathbf{p}^0 . The results of numerical simulations shown in Fig. 6 indicate that the aperiodic structure is more sensitive than the 5×5 finite-sized periodic array. With increasing L , the standard deviation of J' for the aperiodic lattice increases faster than for the 5×5 finite-sized periodic array. The standard deviation initially increases as $\sigma(J') = 0.0524L/\lambda_0$ for the 5×5 finite-sized periodic array while for the aperiodic structure with 50 cylinders $\sigma(J') = 0.1369L/\lambda_0$. The greater sensitivity of the aperiodic design suggests competition between device performance and robustness. Hard to achieve functionality such as the top-hat objective function described in Sec. V results in a higher sensitivity to small perturbations than the 5×5 finite-sized periodic array.

Figure 6 shows saturation of $\sigma(J')$ for large L . We investigated this asymptotic behavior by considering the statistical properties of the power profile $s_{\text{mod}}(\theta_k, \mathbf{p}^{\text{rand}})$ for randomly positioned, nonoverlapping, configurations \mathbf{p}^{rand} in the EM dielectric scattering domain of size L_{max} . The limiting values for $\sigma(J')$ are 0.017 similar to the values for $L/\lambda_0 = 0.8$ shown in Fig. 6.

VI. CONCLUSIONS

Using a computationally efficient gradient-based optimizer and finite difference forward solver we have demon-

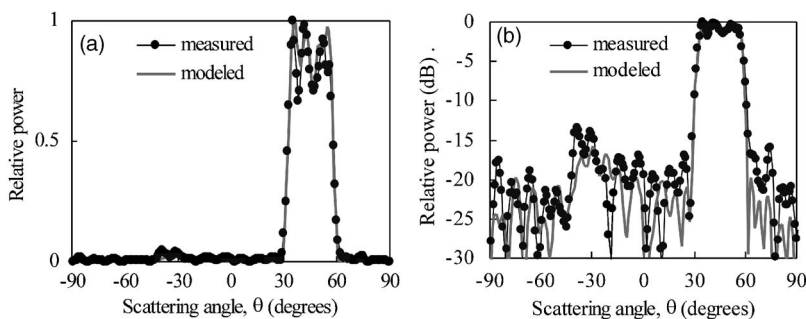


FIG. 5. (a) Calculated and measured EM power profile along measurement curve. The relative power scale is linear. (b) Same as (a) but relative power scale is in decibels. Ripples at the top-hat peak are approximately 1.77 dB peak to peak. The portion of the measured power focused between scattering angles $30^\circ \leq \theta \leq 60^\circ$ in the range $-90^\circ \leq \theta \leq 90^\circ$ is 92.37%.

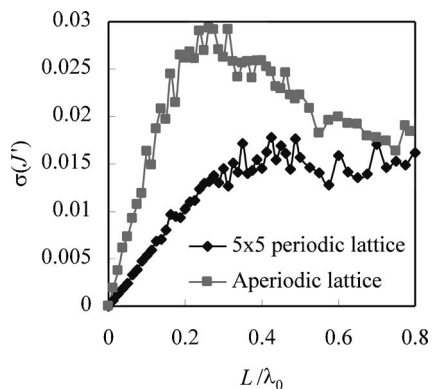


FIG. 6. Sample deviation $\sigma(J')$ as a function of L . Power profile was evaluated using the cost functional $J' = [\sum_{i=1}^M (s_i - s_{0,i})^2]^{1/2}$ for uniform perturbations of size L as in (a). Each point represents the standard deviation of a sample of 200 randomly perturbed parameter settings. The 5×5 finite-sized periodic array increases with L until it reaches its limiting value for randomly distributed scattering cylinders, while the aperiodic lattice peaks before settling down to its limiting value.

strated that the spatial arrangement of identical parallel dielectric cylinders may be configured to closely match a desired EM response. We find good agreement between calculations and experiments for an objective function in which EM radiation propagating in the $\theta=0^\circ$ direction is scattered

into a top-hat function whose peak occurs in the angular range $30^\circ \leq \theta \leq 60^\circ$ on a measurement curve. The spatial arrangement of scattering cylinders is aperiodic and nonintuitive. The methodology we have described extends the functionality of rf and nanophotonic devices beyond that of PC inspired designs.

ACKNOWLEDGMENTS

We thank M. Hossein-Zadeh for helpful discussions. This work is supported by DARPA.

¹J. D. Joannopoulos, R. D. Mead, and J. N. Winn, *Photonic Crystals* (Princeton University Press, Princeton, 1995).

²For example, S. J. McNab, N. Moll, and Y. A. Vlasov, *Opt. Express* **11**, 2927 (2003); Y. Du and A. F. J. Levi, *Solid-State Electron.* **47**, 1369 (2003).

³J. M. Geremia, J. Williams, and H. Mabuchi, *Phys. Rev. E* **66**, 066606 (2002).

⁴L. Sanchis, A. Håkansson, D. López-Zanón, J. Bravo-Abad, and J. Sánchez-Dehesa, *Appl. Phys. Lett.* **84**, 4460 (2004).

⁵A. Håkansson, J. Sánchez-Dehesa, and L. Sanchis, *IEEE J. Sel. Areas Commun.* **23**, 1365 (2005).

⁶Y. Jiao, S. Fan, and D. A. B. Miller, *Opt. Lett.* **30**, 141 (2005).

⁷I. L. Gheorma, S. Haas, and A. F. J. Levi, *J. Appl. Phys.* **95**, 1420 (2004).

⁸D. M. Kingsland, J. Gong, J. L. Volakis, and J.-F. Lee, *IEEE Trans. Antennas Propag.* **44**, 975 (1996).

⁹J.-P. Berenger, *J. Comput. Phys.* **127**, 363 (1996).